Medical Physics
The International Journal of Medical Physics Research and Practice

Evaluation of a silicon photomultiplier PET insert for simultaneous PET and MR imaging

Guen Bae Ko, Kyeong Yun Kim, Hyun Suk Yoon, Min Sun Lee, Jeong-Whan Son, Hyung-Jun Im, and Jae Sung Lee

Citation: Medical Physics **43**, 72 (2016); doi: 10.1118/1.4937784
View online: http://dx.doi.org/10.1118/1.4937784
View Table of Contents: http://scitation.aip.org/content/aapm/journal/medphys/43/1?ver=pdfcov
Published by the American Association of Physicists in Medicine

Evaluation of a silicon photomultiplier PET insert for simultaneous PET and MR imaging

Guen Bae Ko, Kyeong Yun Kim, and Hyun Suk Yoon
Department of Nuclear Medicine, Seoul National University College of Medicine, Seoul 110-799, South Korea and Department of Biomedical Sciences, Seoul National University College of Medicine, Seoul 110-799, South Korea

Min Sun Lee
Department of Nuclear Medicine, Seoul National University College of Medicine, Seoul 110-799, South Korea and Interdisciplinary Program in Radiation Applied Life Science, Seoul National University College of Medicine, Seoul 110-799, South Korea

Jeong-Whan Son
Department of Nuclear Medicine, Seoul National University College of Medicine, Seoul 110-799, South Korea and Department of Biomedical Sciences, Seoul National University College of Medicine, Seoul 110-799, South Korea

Hyung-Jun Im
Department of Nuclear Medicine, Seoul National University College of Medicine, Seoul 110-799, South Korea

Jae Sung Lee[a)]
Department of Nuclear Medicine, Seoul National University College of Medicine, Seoul 110-799, South Korea; Department of Biomedical Sciences, Seoul National University College of Medicine, Seoul 110-799, South Korea; Interdisciplinary Program in Radiation Applied Life Science, Seoul National University College of Medicine, Seoul 110-799, South Korea; and Institute of Radiation Medicine, Medical Research Center, Seoul National University College of Medicine, Seoul 110-799, South Korea

(Received 3 August 2015; revised 8 November 2015; accepted for publication 16 November 2015; published 21 December 2015)

Purpose: In this study, the authors present a silicon photomultiplier (SiPM)-based positron emission tomography (PET) insert dedicated to small animal imaging with high system performance and robustness to temperature change.
Methods: The insert consists of 64 LYSO-SiPM detector blocks arranged in 4 rings of 16 detector blocks to yield a ring diameter of 64 mm and axial field of view of 55 mm. Each detector block consists of a 9×9 array of LYSO crystals ($1.2\times1.2\times10$ mm^3) and a monolithic 4×4 SiPM array. The temperature of each monolithic SiPM is monitored, and the proper bias voltage is applied according to the temperature reading in real time to maintain uniform performance. The performance of this PET insert was characterized using National Electrical Manufacturers Association NU 4-2008 standards, and its feasibility was evaluated through *in vivo* mouse imaging studies.
Results: The PET insert had a peak sensitivity of 3.4% and volumetric spatial resolutions of 1.92 (filtered back projection) and 0.53 (ordered subset expectation maximization) mm^3 at center. The peak noise equivalent count rate and scatter fraction were 42.4 kcps at 15.08 MBq and 16.5%, respectively. By applying the real-time bias voltage adjustment, an energy resolution of $14.2\%\pm0.3\%$ was maintained and the count rate varied $\leq1.2\%$, despite severe temperature changes (10–30 °C). The mouse imaging studies demonstrate that this PET insert can produce high-quality images useful for imaging studies on the small animals.
Conclusions: The developed MR-compatible PET insert is designed for insertion into a narrow-bore magnetic resonance imaging scanner, and it provides excellent imaging performance for PET/MR preclinical studies. © *2016 American Association of Physicists in Medicine.* [http://dx.doi.org/10.1118/1.4937784]

Key words: molecular imaging, PET/MRI, silicon photomultiplier (SiPM), hybrid imaging, animal imaging

1. INTRODUCTION

Positron emission tomography (PET) is a useful biomedical imaging tool allowing the visualization of physiological, biochemical, and molecular processes *in vivo*.[1–5] The usefulness of PET data can be augmented by morphological information from an anatomic imaging modality, such as computed tomography (CT) and, more recently, magnetic resonance imaging (MRI).[6–9]

PET/MRI has received a great deal of attention over the past decade in both the clinical and preclinical imaging fields due to its emerging application in various fields

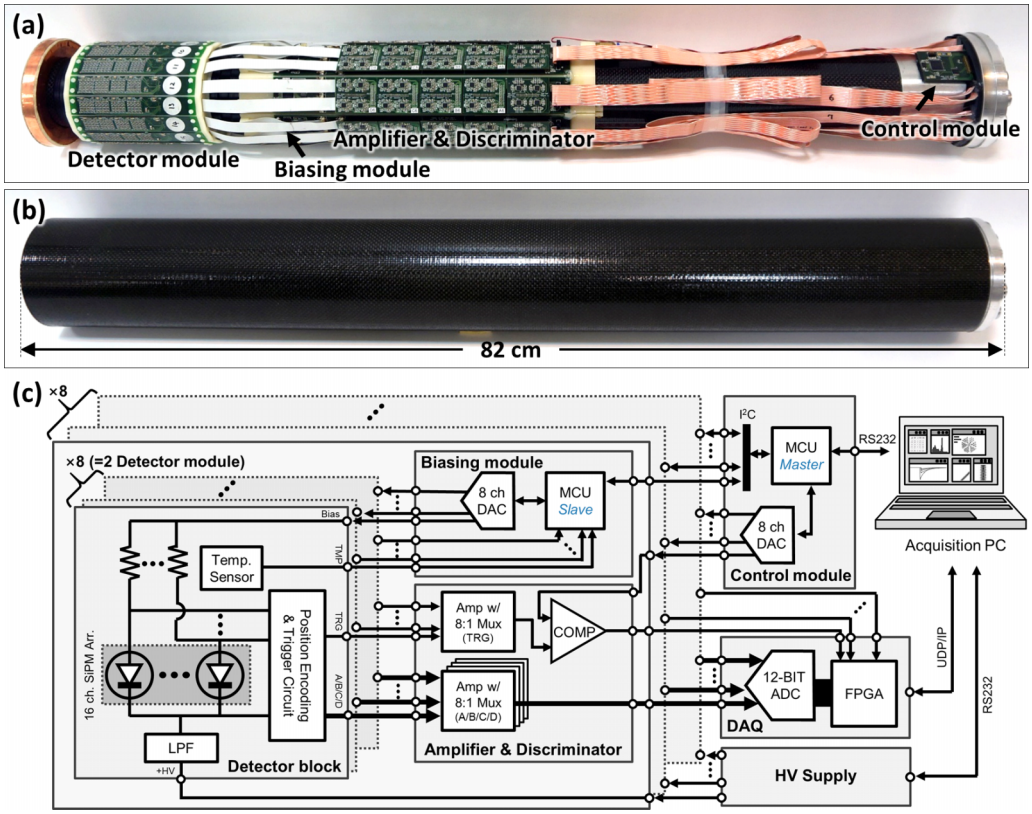

FIG. 1. Photograph of the SiPM PET insert (a) without and (b) with outer cover. (c) Schematic drawing of the whole SiPM PET apparatus showing the detector blocks, biasing modules, amplifiers, discriminators, control module, and data acquisition system.

including oncology,[10,11] neurology,[12,13] and cardiology.[14] Recent advances in semiconductor photosensors such as the avalanche photodiode (APD) and silicon photomultiplier (SiPM) have facilitated the development of PET/MRI, thanks to their compact size and magnetic field insensitivity.[15–20] These characteristics enable the photosensors to be coupled with the scintillation crystals directly in the presence of a magnetic field,[19,21,22] although the relatively short optical fiber bundles inserted between them are regarded useful for minimizing mutual interference between the PET and MRI systems.[16,23,24] In recent years, much research has focused on SiPM rather than APD, because SiPM offers time-of-flight measurement capability due to its superb amplification gain and faster response time.[25–28]

Previous studies have demonstrated the feasibility of SiPM for preclinical PET/MRI research.[19,20] However, there remains a need for the PET systems with specification, performance, and stability so that high-quality images of short-lived radiotracers can be obtained and short time-interval dynamic studies performed.[29] Better system design and integration to minimize the size of PET detectors and front-end electronics are also required to enable the combination of PET system (or PET insert) with small animal dedicated high-field MRI machines providing better system performance and availability for animal studies. Maintaining system performance despite variations in temperature is another challenge of SiPM-based systems, particularly those with PET inserts placed inside the MRI machine.

We have previously reported on our developments of a SiPM-based MRI-compatible preclinical PET system that has a relatively long axial field of view (FOV) and high spatial resolution optimized for small animal imaging.[30,31] We designed this PET system to be inserted inside small diameter (MR opening ~10 cm) and ultrahigh field (>7 T) MRI and to operate reliably without active cooling, while the systems presented in some recent developments were integrated with 3 T large-bore MRI (>60 cm) and needed liquid cooling.[32,33] Here, we present the SiPM system, report the results of PET performance evaluation according to National Electrical Manufacturers Association (NEMA) NU 4-2008 standard methods,[34] and demonstrate its use in some

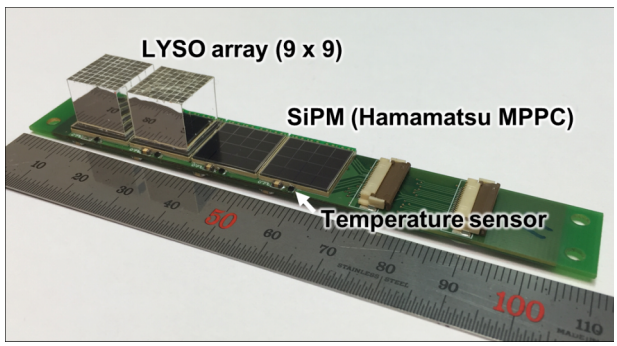

FIG. 2. PET detector module supporting four detector blocks. Two crystal blocks have been removed for the better visualization of the SiPM arrays.

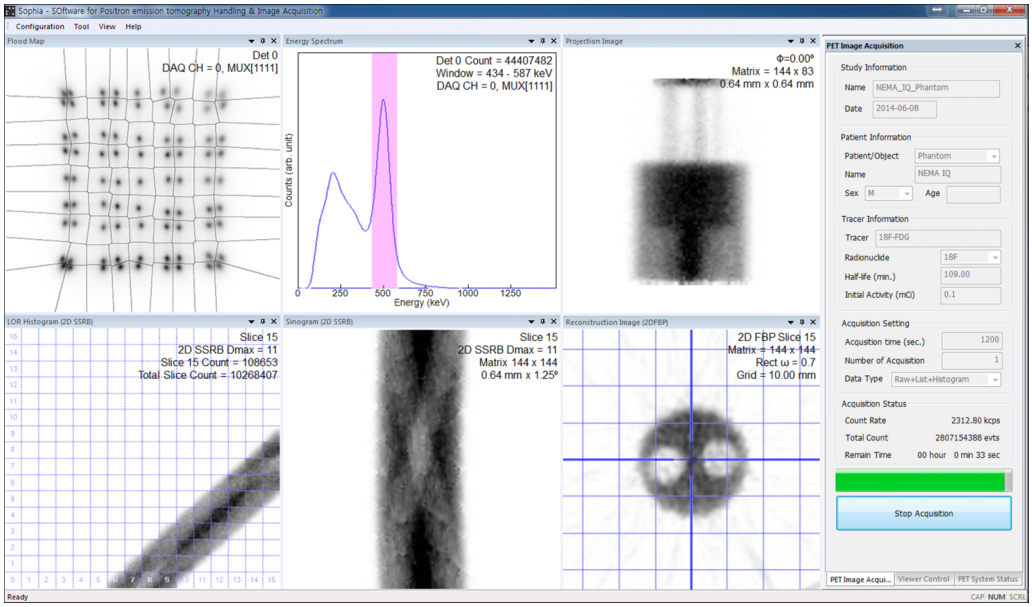

FIG. 3. PET system management and data acquisition software, SOPHIA.

in vivo PET imaging studies. We also demonstrate how temperature-compensation of the SiPM bias voltage makes the performance of the PET system robust to changes in detector temperature.

2. MATERIALS AND METHODS

2.A. MR-compatible PET scanner

The SiPM PET system consists of detector modules, biasing modules, amplifiers, discriminators, and a control module [Figs. 1(a) and 1(c)]. The 16 detector modules and other electronics were arranged in a ring shape supported by a three-dimensional (3D) printed acrylonitrile butadiene styrene frame (Mojo, Stratasys, Ltd., Eden Prairie, MN, USA). We mounted the frame on a carbon fiber tube [inner/outer diameters (ID/OD), 60/62 mm] for the purpose of electromagnetic shielding and mechanical support. Another carbon fiber tube (ID/OD, 98/100 mm) optically and electromagnetically shielded the PET insert [Fig. 1(b)]. An axial FOV of 55 mm and a ring diameter of 64 mm were achieved, which is most suitable for mouse imaging.

2.A.1. Detector module

The PET detector module, populated with a nonmagnetic passive component, supports four detector blocks (Fig. 2). Each detector block consists of a 9×9 array of LYSO crystals (SIPAT, Chongqing, China) and a monolithic 4×4 SiPM array (S11828-3344M; Hamamatsu Photonics K.K., Hamamatsu, Japan). An enhanced spectral reflector polymer (3M Company, Maplewood, MN, USA) with 0.065-mm thickness was used to construct the crystal array and optically isolate each LYSO crystal with a dimension of $1.2\times1.2\times10$ mm^3, yielding a crystal pitch of 1.28 mm. The anodes of each monolithic SiPM array were fed into a resistive charge division network to reduce the number of readout signal lines from sixteen to four.[35] Microsize temperature sensors were attached next to each SiPM array for monitoring the temperature change in the SiPM.

2.A.2. Biasing module

One of the major challenges in SiPM-based PET system is achieving performance stability despite variations in temperature and bias voltage.[36] Therefore, we developed

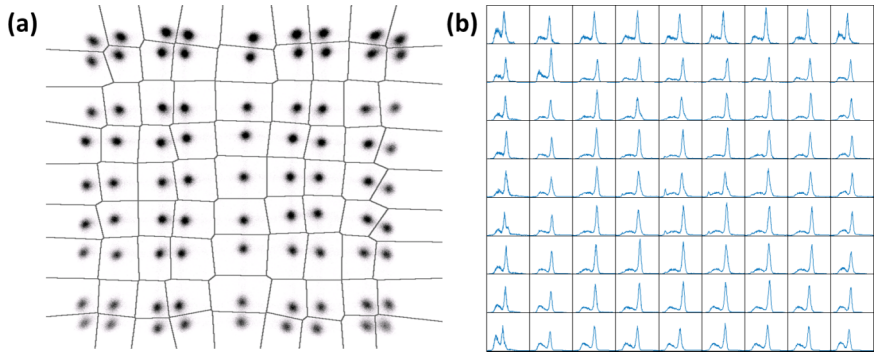

FIG. 4. Intrinsic properties of a representative detector block. (a) Flood image with fishnet. (b) Energy spectra of all 81 crystals in the detector block.

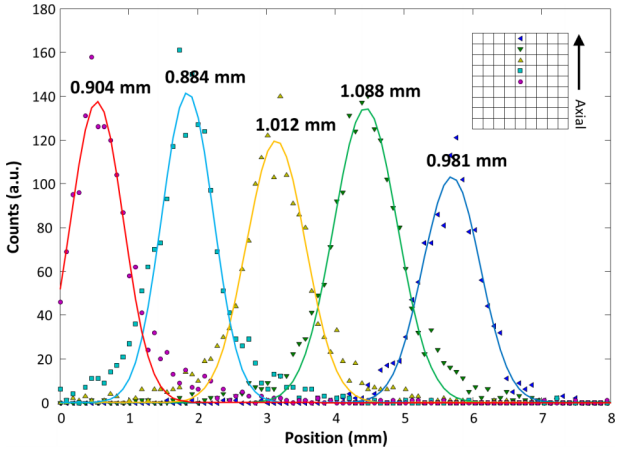

FIG. 5. Intrinsic spatial resolution profile of the detector block. Average, best, and worst intrinsic resolutions are 0.974, 0.884, and 1.088 mm FWHM, respectively.

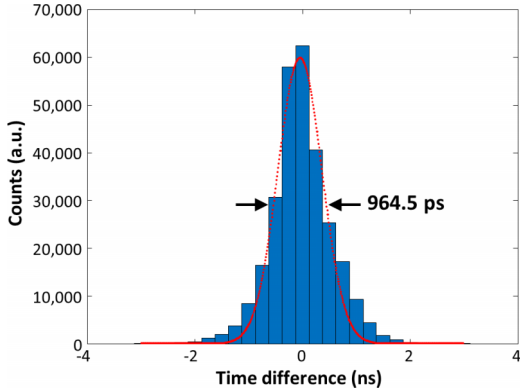

FIG. 6. Timing spectrum obtained using a representative SiPM detector block and a LYSO-fast PMT reference detector.

a biasing module to yield fine adjustments and precise monitoring of applied bias voltage according to temperature variation. One biasing module consisting of a microcontroller unit and an 8-channel 12-bit digital-to-analog converter supports eight detector blocks (i.e., two detector modules). The gain chosen for each SiPM was that which yielded the best values of energy resolution and quality of flood image for the detector blocks at 2 °C, where the quality of flood image was defined as the ratio of the separation between two adjacent spots in the flood image to the average width of the two spots.[37]

2.A.3. Amplifier and discriminator

The multiplexed position signals were transferred to low power differential amplifiers through 20 cm flat flexible cables, minimizing heat transfer into the detector modules. The gain of the amplifier was determined to match the input dynamic range of the data acquisition (DAQ) system. The AC-coupled common cathode signals were amplified by fast current-feedback operational amplifiers to prevent the degradation of timing performance. The signals from eight detector blocks were further multiplexed to one detector signal (8:1) by bipolar multiplexing, which encodes each detector to the combination of polarities of four position signals.[38] The trigger signal for the DAQ was generated through an analog comparator by comparing the magnified common-cathode signal to a predetermined threshold voltage. The total power consumption by the amplifiers was less than 5 W for the entire system.

2.A.4. Control module, data acquisition board, and acquisition software

The role of the control module is to set the threshold voltages of comparators in discriminators and communicate with biasing modules and with a data acquisition computer. The bias voltage and current and temperature of each detector block were monitored and controlled in real time by a custom-built acquisition and system management software tool named software for positron emission tomography handling and image acquisition (SOPHIA). The discriminator threshold voltages for the multiplexed signals (signals after bipolar multiplexing) were also adjusted individually using the SOPHIA software; several variables, such as expected dark current and count rates, were taken into account. In this study, we chose optimized threshold for each multiplexed signal to avoid false trigger and minimize time walk error.

The signals from the amplifiers and discriminators are acquired and processed by a custom-made field-programmable gate array (FPGA)-based DAQ board. When a trigger signal is detected, the position signals are sampled by 12-bit 125 MHz analog-to-digital converters, and the triggered DAQ channel number and arrival time information are recorded. Information on single gamma events was transferred to a PC

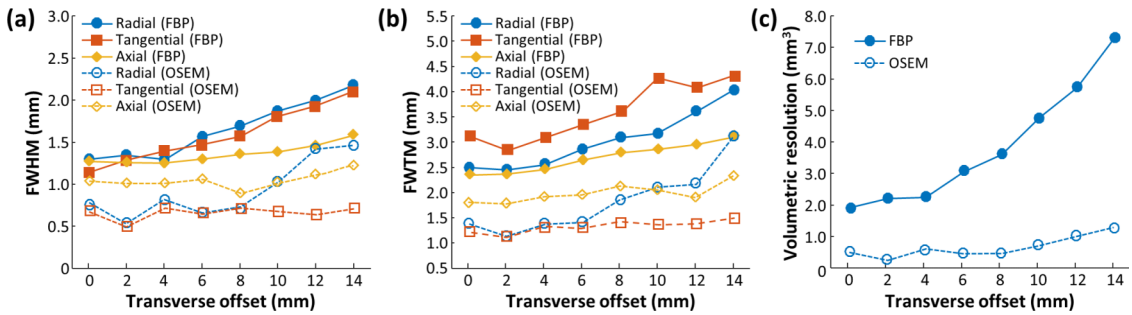

FIG. 7. Reconstructed image spatial resolution of the SiPM PET as a function of transverse offset from the center of the FOV. (a) FWHM, (b) FWTM, and (c) volumetric resolution.

TABLE I. Summary of spatial resolution results.

Reconstruction method	At center			At 14 mm		
	Radial	Tangential	Axial	Radial	Tangential	Axial
FBP	1.31	1.14	1.29	2.18	2.11	1.58
OSEM	0.75	0.68	1.05	1.46	0.71	1.22

via a 1-gigabit Ethernet. The acquisition software, SOPHIA, processed the single-event information and generated list-mode data of coincidence and 3D line-of-response (LOR) histograms of prompt and random coincidence events in real time. The energy and timing windows were set to 350–650 keV and 12 ns unless otherwise stated, and the random coincidence was estimated from the single-event rate. The timing window was set to 12 ns, which is ~9 times wider than reported coincidence time resolution of detector block (see Sec. 3.A), at the expense of time resolution in order to take the time offset between signal channels due to the signal cable and FPGA routing path length difference into account. The raw data transferred from DAQ were saved for retrospective processing. The recorded prompt count, input count rate, flood images, energy spectra, LOR histogram, sinogram, projection image, and reconstructed image using 2D filtered back projection (FBP) were displayed and updated every second (Fig. 3).

2.A.5. Image generation

The 3D LOR histograms were corrected for random coincidence and sensitivity variation. All data were reconstructed using LOR-based 3D ordered subset expectation maximization (OSEM) with 3 iterations and 12 subsets and postsmoothed using a 1-mm full-width at half-maximum (FWHM) 3D Gaussian kernel. For the evaluation of PET system spatial resolution, the LOR histogram data were converted into sinogram and single slice rebinning and FBP reconstruction was applied additionally.

2.B. Detector performance evaluation

Flood images and energy spectra of all 64 detector blocks were obtained by irradiating them for an hour with a ^{22}Na point source (activity = 0.18 MBq) located at the center of PET FOV. The intrinsic spatial resolutions of a representative detector pair were measured at the transaxial center by moving the same point source in the axial direction with a step size of 0.2 mm from the center to the edge of the detector pair. The time resolution of a representative detector block was measured using a reference detector module consisting of LYSO crystal and fast PMT (Ref. 39) and a commercial Nuclear Instrumentation Modules/Versa Module Eurocard data acquisition setup. Then, the predicted coincidence time resolution of detector block was calculated by quadratically subtracting the time uncertainty of the reference PMT (~200 ps) from the measured time resolution with the reference detector and multiplying by $\sqrt{2}$.

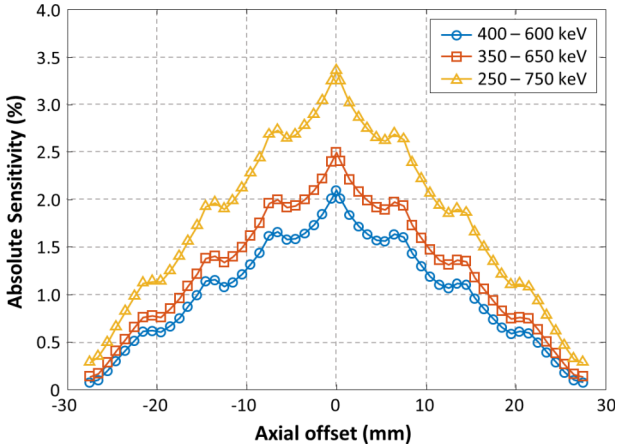

FIG. 8. Sensitivity profile over axial positions applying various energy windows.

2.C. NEMA NU 4-2008 performance evaluation

2.C.1. Spatial resolution

A 0.18 MBq ^{22}Na point source with a 0.25-mm diameter of sphere nominal active area embedded in a 1×0.25 in. (diameter × height) acrylic cylinder was used for the measurement of spatial resolution. The data acquired with the source located at the axial center of one detector ring were reconstructed using FBP and OSEM algorithm without any smoothing. The radial, tangential, and axial resolutions at

TABLE II. Summary of count-rate performance test results.

Energy window (keV)	Time window (ns)	Peak true (kcps)	Activity (MBq)	Peak NECR (kcps)	Activity (MBq)	NECR 3.7 MBq (kcps)	Scatter fraction (%)
400–600	4	15.71	13.48	12.91	11.50	8.23	5.87
	8	28.27	13.77	22.85	11.79	14.27	6.20
	12	36.57	15.81	28.61	12.13	17.36	6.68
350–650	4	19.86	15.41	15.29	12.18	9.31	9.17
	8	36.20	15.94	27.30	12.98	16.25	9.68
	12	47.66	18.21	34.68	13.41	19.96	10.46
250–750	4	26.21	18.24	17.98	13.42	10.46	14.42
	8	48.76	18.48	32.58	13.50	18.56	15.27
	12	65.95	19.04	42.41	15.03	23.40	16.53

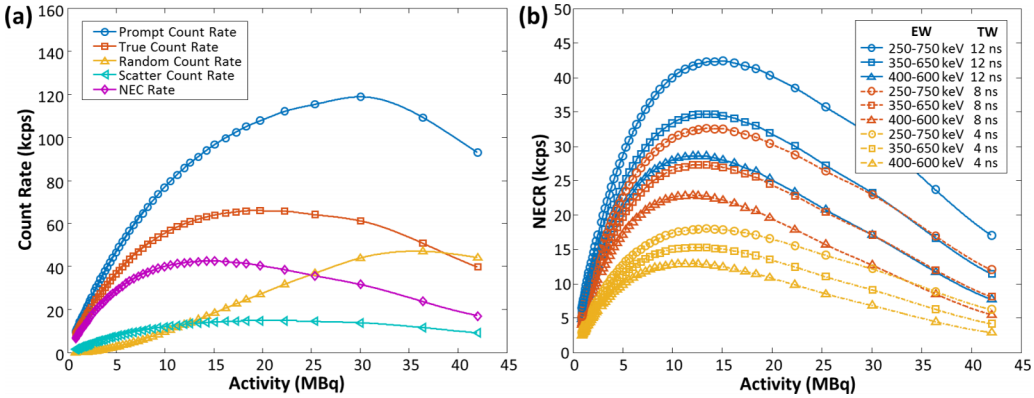

FIG. 9. Count rate performance. (a) Plot of prompt count rate, true count rate, random count rate, scatter count rate, and NECR versus activity for mouse-sized phantom with a coincidence time window of 12 ns and an energy window of 250–750 keV. (b) Plot of NECR as a function of energy window and time window setting.

radial distances of 0, 2, 4, 6, 8, 10, 12, and 14 mm from the center were measured and reported as a FWHM and full-width at tenth-maximum (FWTM).

2.C.2. Sensitivity

The axial sensitivity profile was measured with the same point source used for spatial resolution measurement moving through the axis of PET cylinder with a 0.64-mm step size (half crystal pitch). Data acquired at each position were processed with the energy windows of 400–600, 350–650, and 250–750 keV to investigate the dependence of sensitivity on the energy window. For each sinogram, pixels located within 1 cm from the peaks were used to calculate sensitivities as described in the NEMA NU 4-2008 protocol. The absolute sensitivities corrected for by the branching ratio of ^{22}Na (% unit) are reported in this paper. The total absolute sensitivity calculated as the average absolute sensitivity over the entire axial FOV is reported.

2.C.3. Scatter fraction, count losses, and random coincidence measurement

A mouse-sized phantom (70-mm length and 25-mm diameter) made of high-density polyethylene (0.96 g/cm^3) was used for count rate performance measurement. A flexible tube containing ^{18}F solution was inserted into a 3.2-mm diameter cylindrical hole located 10 mm away from the central axis of the phantom. The phantom was scanned every 20 min for 5 min with an initial activity of 42 MBq at the start of acquisition until the total activity decayed below 0.5 MBq. The acquired data were processed as described in the NEMA NU 4-2008 protocol, and intrinsic counts were estimated from data acquired with a cold mouse-sized phantom for 24 h.

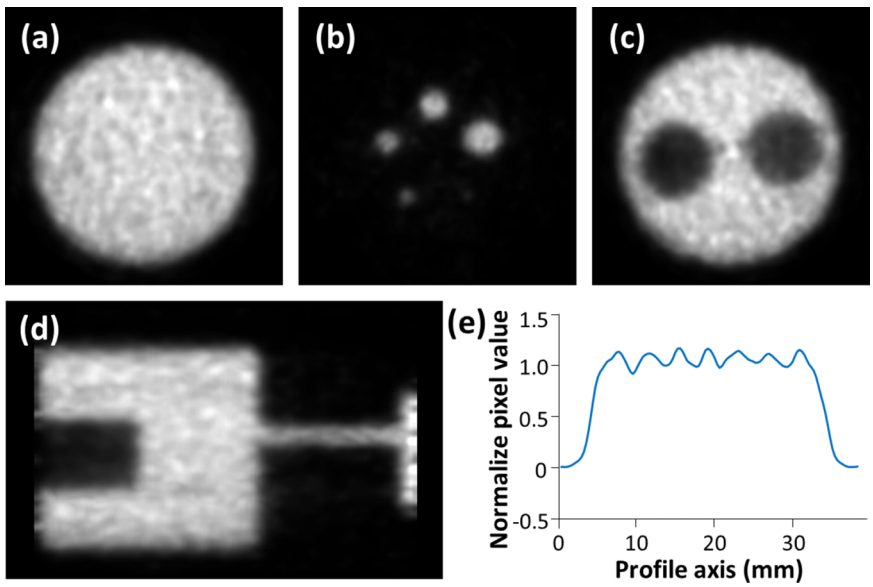

FIG. 10. Reconstructed images of NEMA NU-4 IQ phantom. (a) Transverse slice of the uniform region. (b) Transverse slice of the rod region. (c) Transverse slice of the cold chamber region. (d) Coronal slice of the phantom. (e) Pixel intensity profile across uniform area. Intensity scale is set so that the minimum value is 0 and the maximum value is 1.25 times the mean value of the uniform cylinder region.

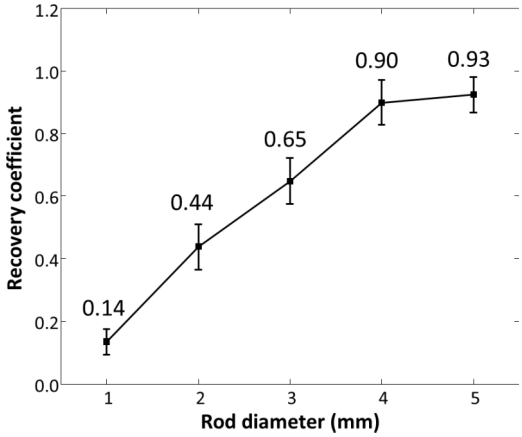

FIG. 11. Recovery coefficients and standard deviations for five rods of different sizes ranging between 1 and 5 mm.

Count-rate plot, peak count rate values, and system scatter fraction are reported for several energy and time window settings.

2.C.4. *Image quality*

The NEMA image quality (IQ) phantom filled with 3.7 MBq of 2-deoxy-2-[^{18}F]fluoro-D-glucose ([^{18}F]FDG) solution was scanned for 20 min to evaluate image quality. One of the cold region chambers was filled with nonradioactive water, and the other was filled with air. Random and normalization corrections were applied to the data. The uniformity of a 22.5-mm-diameter and a 10-mm-long cylindrical volume on the uniform region, recovery coefficients of the averaged 10-mm-long hot-rod images, and the spill-over ratio of the volume on the cold region were evaluated.

2.D. Temperature-dependent stability

To evaluate the stability of the SiPM PET system over a wide temperature range, a PET insert was installed in a temperature control box (CT-BDI150; Coretech, Anyang, Korea). While the temperature inside of the box was continuously increased from 5 to 35 °C, two different measurements were conducted with a ^{22}Na point source located at the center of FOV: one measurement using the SiPM operated with a fixed bias voltage that was optimized at 20 °C and the other one using the SiPM operated with an automatically regulated bias voltage supplied from the real-time adjustment system. Energy peak positions and resolutions were measured at a number of different temperatures between 10 and 30 °C, and the composite energy spectra were measured from data collected during temperature excursions of 19.5–20.5, 19–21, and 10–30 °C. PET count rates were obtained by applying three different energy windows (400–600, 350–650, and 250–750 keV) at every 0.2 °C interval between 18 and 22 °C.

2.E. *In vivo* imaging studies

To show the feasibility of this SiPM PET system, two mouse imaging studies were performed. All animal experiments were approved and conducted in accordance with guidelines established by the Institutional Animal Care and Use Committee at the Seoul National University Hospital.

We intravenously injected 12.4 MBq/0.2 ml [^{18}F]FDG via a tail vein into a BALB/c mouse (21.4 g) under isoflurane anesthesia. After a 30-min tracer-uptake period, whole-body PET images were acquired for 45 min without moving the bed position.

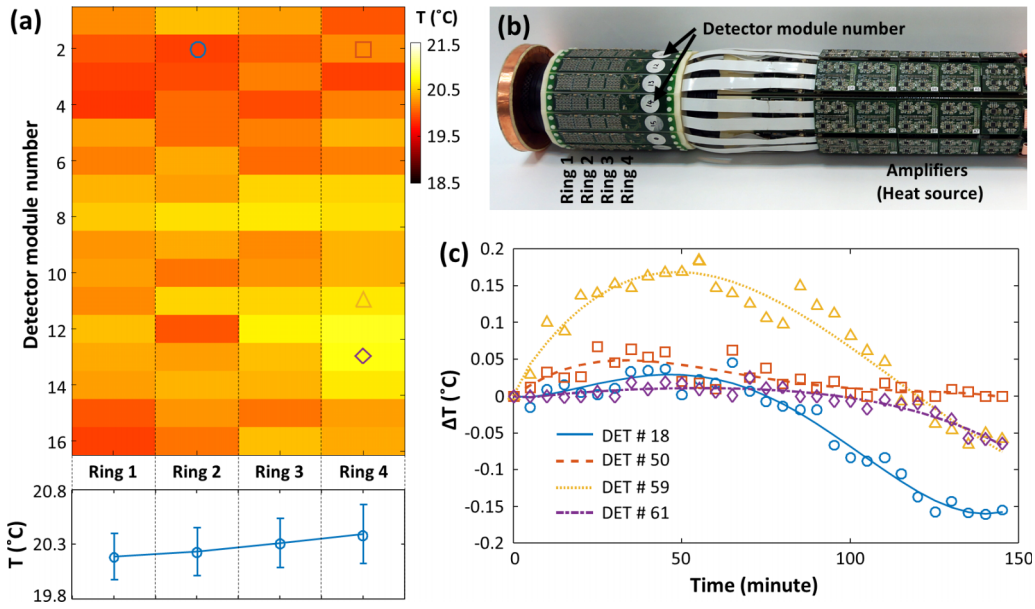

FIG. 12. PET detector performance depending on temperature variation. (a) Temperature distribution of 64 SiPMs (top) and plot of average temperature in the same block ring (bottom) measured when a 0.18 MBq ^{22}Na point source was scanned in a thermostatic chamber. The apparent temperatures tend to be higher at the SiPMs located close to the amplifiers (ring 4) than those located away from the amplifiers. (b) Picture showing the locations of SiPMs and amplifiers. (c) Temperature variation of four selected SiPMs. The position of each sensor is denoted in (a) by symbols.

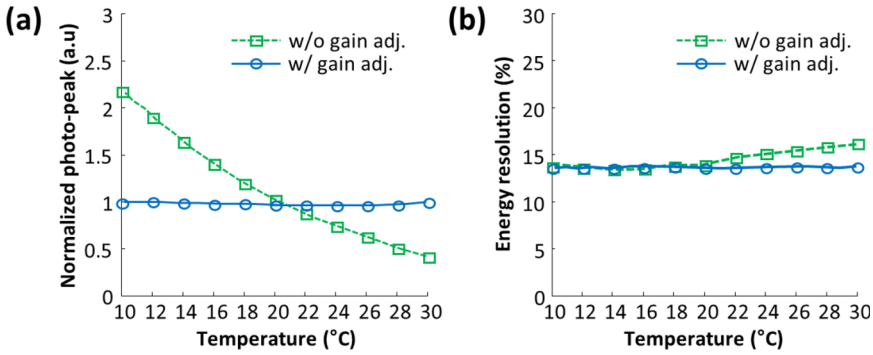

FIG. 13. (a) Photo-peak positions at various temperatures with and without applying bias voltage compensation. (b) Average energy resolutions at various temperatures with and without applying bias voltage compensation.

We also examine dopamine transporter density in a Parkinson disease (PD) mouse model using N-(3-[^{18}F]fluoropropyl)-2β-carbomethoxy-3β-(4-iodophenyl)nortropane ([^{18}F]FP-CIT) as a tracer. The PD mouse model was induced by unilateral injection of 6-hydroxydopamine (6-OHDA) into the right striatum.[40] A total of 14.8 MBq [^{18}F]FP-CIT was injected into the PD mouse (27.7 g) and normal control mouse (24.4 g). Before PET imaging, a CT scan was performed using GE eXplore VISTA PET/CT scanner. Then, the mice and animal bed were manually transferred to the SiPM PET device. Great care was taken to ensure that the posture of the animals was not changed. After a 70-min uptake period, PET images were acquired for 30 min for each mouse. Image fusion of SiPM PET and x-ray CT was performed after spatial registration with a rigid-body transformation between them using FIRE software.[41]

3. RESULTS

3.A. Detector performance

All of the 1.2-mm crystals in the flood image were clearly resolved, even in the edge region of the crystal array [Fig. 4(a)]. The energy resolution for 511-keV gamma ray photons was 14.2% ± 2.0% on average for entire 5184 crystal elements used in the system (best and worst resolutions were 10.5% and 28.9%, respectively); the energy spectra of the crystals in a representative block are shown in Fig. 4(b). The intrinsic spatial resolution was 0.974 mm on average in a pair of two representative detector blocks. The best and worst values were 0.884 and 1.088 mm, respectively (Fig. 5). The measured time resolution of a representative SiPM detector block-fast PMT detector pair was 964.5 ps (Fig. 6), and thus the calculated coincidence time resolution of the detector block is 1.33 ns.

3.B. System performance

Spatial resolution results for FBP and OSEM are summarized in Fig. 7 and numeric results at the center of the FOV and 14 mm off-center are reported in Table I. The volumetric resolutions for FBP and OSEM at the center of the FOV were 1.92 and 0.53 mm^3, respectively.

The absolute peak sensitivities were measured with a coincidence time window of 12 ns and an energy window of 250–750, 350–650, and 400–600 keV and resulted in 3.36%, 2.50%, and 2.11%, respectively. The total absolute sensitivities, calculated as the average absolute sensitivity over the entire axial FOV, were 1.80%, 1.28%, and 1.05% for each energy window. The overall sensitivity profile is triangular-shaped, as expected, with small bumps at the center of the detector block and in the gap between detector blocks (Fig. 8). With the energy window of 250–750 keV and a coincidence time window of 12 ns, the peak noise equivalent count rate (NECR) and scatter fraction were 42.4 kcps (at 15.0 MBq) and 16.5% (Table II and Fig. 9). The standard deviation of pixel values in the uniform region of a NEMA IQ phantom was 6.19% [Figs. 10(a) and 10(e)], and the recovery coefficients of five different hot-rods were 0.14, 0.44, 0.65, 0.90, and 0.93 for a 1-, 2-, 3-, 4-, and 5-mm rod diameter, respectively [Figs. 10(b) and 11]. The spill-over ratios for air- and water-filled chambers were 17.3% and 8.5%, respectively [Fig. 10(c)].

3.C. Robustness of the SiPM PET system to temperature change

The measured temperatures of the SiPMs used in this system were nonuniform [Fig. 12(a)] and varied irregularly [Fig. 12(c)] even in a thermostatic chamber. The main causes of variable temperatures include the radioactive source

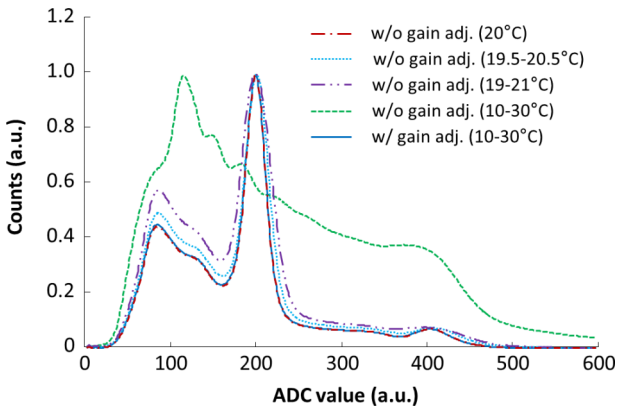

FIG. 14. The effects of temperature variation on energy spectra measured with and without applying bias voltage compensation.

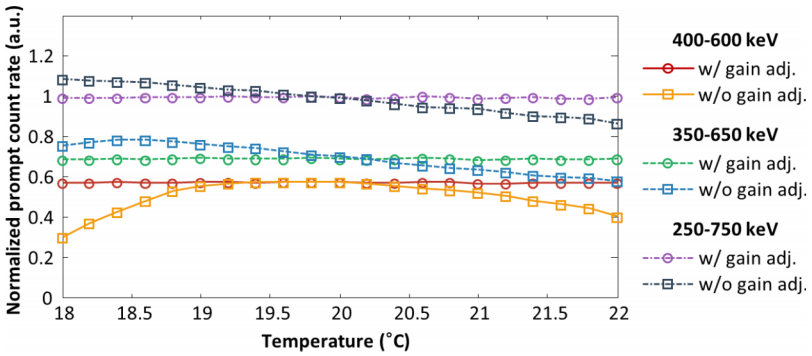

FIG. 15. Prompt count rates according to the apparent temperature and energy window setting. No count rate perturbation is observed with bias voltage compensation (circles).

distribution and heat transfer from amplifiers and electronics [Figs. 12(a) and 12(b)].

Without applying real-time bias voltage adjustment, the photo-peak positions of the PET energy spectra decreased according to the temperature increase with a slope of −5%/°C [squares and dashed lines in Fig. 13(a)]. Slight but gradual degradations in energy resolutions were also observed [squares and dashed lines in Fig. 13(b)]. Moreover, temperature fluctuation of ±0.5 °C (19.5–20.5 °C) and ±1.0 °C (19.0–21.0 °C) resulted in remarkable energy resolution degradation (16.9% and 23.6%, respectively) while 14.2% energy resolution was observed when the temperature was constant at 20 °C (Fig. 14). The broadening of the energy spectrum also led to an increased count rate variation. The count rate variation with the fixed bias voltage but with unstable apparent temperature depended on the width of the energy window (Fig. 15). The maximum count rate changes based on a ±1.0 °C temperature fluctuation for 400–600, 350–650, and 250–750 keV energy windows were 8.9%, 9.4%, and 5.5%, respectively, relative to the count rate at

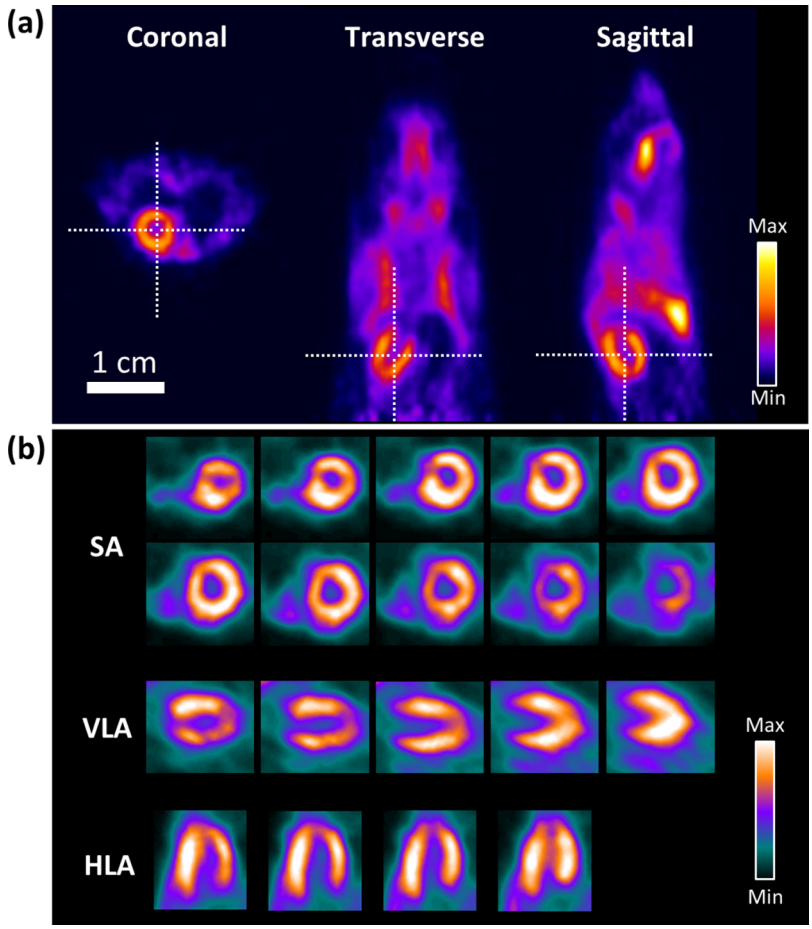

FIG. 16. Images of a BALB/c mouse acquired using [^{18}F]FDG and SiPM PET. (a) Whole-body PET images. Tissues with high glucose utilization rates are visible. (b) Magnified left ventricular slices. Myocardial [^{18}F]FDG uptake is clearly shown in the short axis (upper row), vertical long axis (middle row), and horizontal long axis (lower row).

20 °C, and those based on a ±2.0 °C fluctuation were 47.4%, 17.6%, and 13.0%. This serious count rate instability with fixed bias voltage can cause significant quantification error in PET studies with incorrect calibration factors. However, the real-time adjustment of bias voltage yielded very stable photopeak positions and energy resolutions over a wide temperature range (circles and solid lines in Fig. 13). Accordingly, we could solve the problems of energy spectrum broadening (14.2% with gain adjustment) and count rate instability (only 1.2% change at 400–600 keV energy window) owing to temperature fluctuation (Figs. 14 and 15).

3.D. *In vivo* studies

Figure 16(a) shows whole-body PET images acquired using the SiPM PET scanner. [^{18}F]FDG uptake is clearly seen in tissues with high glucose utilization, including heart muscle, brown fat, spinal bone marrow, and Harderian glands. Figure 16(b) shows magnified images of the heart region. [^{18}F]FDG uptake in the left ventricular myocardium is clearly delineated in short axis, vertical long axis, and horizontal long axis slices, thanks to the high spatial resolution of SiPM PET.

In the dopamine transporter image of control mouse, the symmetric and normal uptake of [^{18}F]FP-CIT uptake was observed in the bilateral striatum [Fig. 17(a)]. On the other hand, [^{18}F]FP-CIT uptake was lower in 6-OHDA-injected striatum of the PD mouse compared with the homologous contralateral region [Fig. 17(b)].

4. DISCUSSION

The SiPMs are suitable photosensors for small animal dedicated PET/MRI because they are available in arrays with small pixel size and operable in the static and time-varying magnetic field. This new silicon sensor has many other attractive properties, including superior amplification gain and a faster response time than proportional-mode APD. However, its gain strongly depends on the applied reverse bias and temperature. Thus, in this study, we used a self-compensation method to maintain uniform SiPM photon counting gain and showed excellent system stability in terms of energy resolution and prompt count rate.

The SiPM PET system developed here yields high spatial resolution and high sensitivity to meet the demands of the molecular imaging scientists. The NEMA performance evaluation results demonstrated that the SiPM-based PET system developed in this study shows excellent imaging performance that is almost comparable to the established PMT-based preclinical PET systems,[42,43] whereas our system also has a compact size and MR-compatibility. Relatively low NECR at high activity level can be improved with some modifications in acquisition electronics.

In this study, complete information of all single gamma events was transferred to a PC using custom-built DAQ and acquisition software. This allows for retrospective processing of the data, which makes it possible to apply different energy and time windows and generate dynamic images for the same data. This method is particularly useful during the development phase, in which many scanning parameters are not optimized. However, the recording of every triggered event, whether detected in coincidence or not, leads to data transmission and storage bottlenecks in the data acquisition system. It is the reason that the NECR peaked with 15 MBq in the phantom; the 1-gigabit Ethernet connection had saturated and events were lost at higher activity levels. This limitation will be solved by the adoption of coincidence detection in the DAQ system.

Bipolar multiplexing is another possible cause of the degradation in count rate performance because the multiplexed detector blocks share readout channels while increasing the probability of pulse pileup.[38] However, the area covering each readout channel (9.33 cm^2 for 8 blocks) is similar to or even smaller than coverage of position sensitive PMT blocks used in state-of-the-art PMT-based small animal PET systems which have outstanding counting rate performances [9 cm^2 for Inveon (Ref. 43) and 39.6 cm^2 for

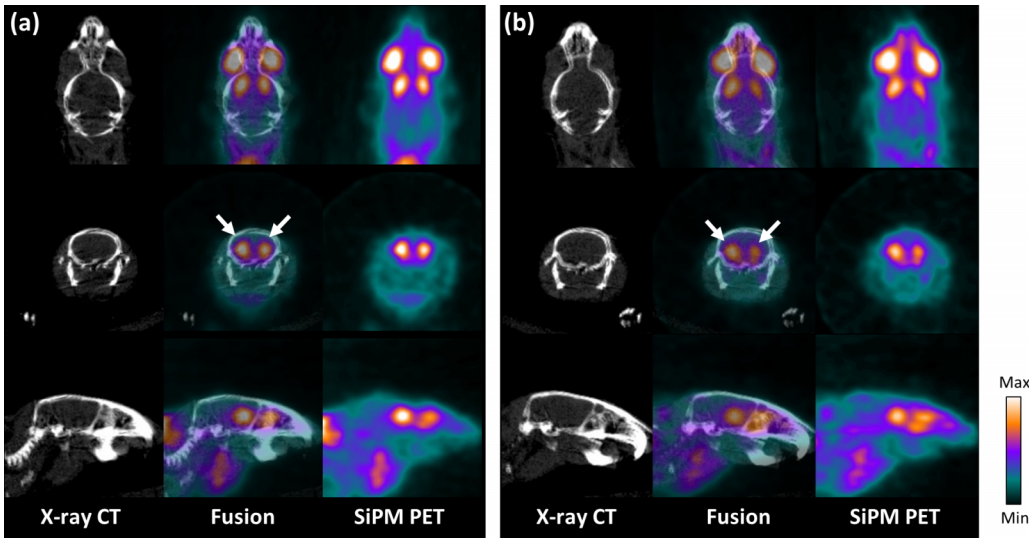

FIG. 17. Dopamine transporter imaging using [^{18}F]FP-CIT in control and PD mice. (a) PET/CT fusion image of a control mouse. (b) PD mouse.

nanoScan PET/MRI (Ref. 44)]. Therefore, the effect appears to be negligible compared to the acquisition electronics.

The stability of the PET system is extremely important for the reliable quantification of activity in comparative or longitudinal studies. Thanks to the low power consumption design (<5 W) and real time bias voltage adjustment, our SiPM PET scanner showed strong performance stability with respect to spatiotemporally varying thermal fluctuations without the need of thermal stabilization for PET detector modules and electronics. Additional active cooling to reduce the temperature would be useful for reducing thermal noise (i.e., dark count of SiPM) and improving detector performance (i.e., timing resolution), and reducing the range of temperature variability using the active cooling would be beneficial in maintaining good intrinsic spatial resolution of detector block. However, the downsides of the active cooling are the slow temperature change response and potential water condensation problem.

The space limitation is another technical challenge in the development of PET insert to be combined with small animal dedicated MRI. We designed the PET system to be installed inside a small bore MRI with an opening as small as 10 cm in diameter. Also, we tried to minimize the thickness of PET electronics to achieve 6-cm inner diameter of PET system. The dimension can accommodate mouse whole-body and rat brain imaging even after the RF coils are placed inside PET, which further reduce the transaxial FOV. An existing commercial preclinical PET/MR system in which the PMT-based PET is combined with 1 T permanent magnet MRI would allow larger transaxial FOV, but only the sequential PET and MR imaging is possible using this system.[44]

We designed the SiPM PET insert to enable the simultaneous scan with MRI.[30,31] Nonmagnetic passive electronics and connectors were used, and the PET insert was optically and electromagnetically shielded by a conducting carbon fiber tube. Because it was previously validated that the carbon fiber shields the radiofrequency signal well and maintains good MRI quality,[16,33] this system is expected to produce high-performance multimodal images if combined with an ultrahigh-field MRI system. The results of mutual interference evaluation between PET and MRI and simultaneous PET/MR imaging will be reported soon in a separate publication.

5. CONCLUSION

We developed a SiPM PET insert for preclinical imaging studies. The results of the NEMA performance evaluation and animal imaging studies show that the performance of the PET insert is comparable with state-of-the-art PMT-based preclinical PET systems.

ACKNOWLEDGMENTS

This work was supported by grants from the National Research Foundation of Korea (NRF) funded by the Korean Ministry of Science, ICT, and Future Planning (Grant No. NRF-2014M3C7034000) and the Korea Health Technology R&D Project through the Korea Health Industry Development Institute (KHIDI), funded by the Ministry of Health and Welfare, Republic of Korea (Grant No. HI14C-0002-030115).

[a]Author to whom correspondence should be addressed. Electronic mail: jaes@snu.ac.kr; Telephone: +82-2-2072-2938; Fax: +82-2-745-2938.

[1]M. E. Phelps, "Positron emission tomography provides molecular imaging of biological processes," Proc. Natl. Acad. Sci. U. S. A. **97**, 9226–9233 (2000).
[2]S. M. Ametamey, M. Honer, and P. A. Schubiger, "Molecular imaging with PET," Chem. Rev. **108**, 1501–1516 (2008).
[3]S. Ha, H. Choi, G. J. Cheon, K. W. Kang, J.-K. Chung, E. E. Kim, and D. S. Lee, "Autoclustering of non-small cell lung carcinoma subtypes on ^{18}F-FDG PET using texture analysis: A preliminary result," Nucl. Med. Mol. Imaging **48**, 278–286 (2014).
[4]I. Lee, S. Y. Knag, C.-Y. Heo, H.-Y. Lee, and S. E. Kim, "Evaluation of flap tissue viability by F-18 FDG PET/CT," Nucl. Med. Mol. Imaging **48**, 241–243 (2014).
[5]S. Lee and H. Park, "Parametric response mapping of longitudinal PET scans and their use in detecting changes in Alzheimer's diseases," Biomed. Eng. Lett. **4**, 73–79 (2014).
[6]T. Beyer, D. W. Townsend, T. Brun, P. E. Kinahan, M. Charron, R. Roddy, J. Jerin, J. Young, L. Byars, and R. Nutt, "A combined PET/CT scanner for clinical oncology," J. Nucl. Med. **41**, 1369–1379 (2000).
[7]D. W. Townsend, "Dual-modality imaging: Combining anatomy and function," J. Nucl. Med. **49**, 938–955 (2008).
[8]S. R. Cherry, "Multimodality imaging: Beyond PET/CT and SPECT/CT," Semin. Nucl. Med. **39**, 348–353 (2009).
[9]J. S. Lee and J. H. Kim, "Recent advances in hybrid molecular imaging systems," Semin. Musculoskeletal Radiol. **18**, 103–122 (2014).
[10]G. Antoch and A. Bockisch, "Combined PET/MRI: A new dimension in whole-body oncology imaging?," Eur. J. Nucl. Med. Mol. Imaging **36**, 113–120 (2009).
[11]A. Boss, S. Bisdas, A. Kolb, M. Hofmann, U. Ernemann, C. D. Claussen, C. Pfannenberg, B. J. Pichler, M. Reimold, and L. Stegger, "Hybrid PET/MRI of intracranial masses: Initial experiences and comparison to PET/CT," J. Nucl. Med. **51**, 1198–1205 (2010).
[12]N. Salamon, J. Kung, S. J. Shaw, J. Koo, S. Koh, and J. Y. Wu, "FDG-PET/MRI coregistration improves detection of cortical dysplasia in patients with epilepsy," Neurology **71**, 1594–1601 (2008).
[13]D. A. Torigian, H. Zaidi, T. C. Kwee, B. Saboury, J. K. Udupa, Z.-H. Cho, and A. Alavi, "PET/MR imaging: Technical aspects and potential clinical applications," Radiology **267**, 26–44 (2013).
[14]W. W. Lee, B. Marinelli, A. M. van der Laan, B. F. Sena, R. Gorbatov, F. Leuschner, P. Dutta, Y. Iwamoto, T. Ueno, M. P. V. Begieneman, H. W. M. Niessen, J. J. Piek, C. Vinegoni, M. J. Pittet, F. K. Swirski, A. Tawakol, M. Di Carli, R. Weissleder, and M. Nahrendorf, "PET/MRI of inflammation in myocardial infarction," J. Am. Coll. Cardiol. **59**, 153–163 (2012).
[15]B. J. Pichler, M. S. Judenhofer, C. Catana, J. H. Walton, M. Kneilling, R. E. Nutt, S. B. Siegel, C. D. Claussen, and S. R. Cherry, "Performance test of an LSO-APD detector in a 7-T MRI scanner for simultaneous PET/MRI," J. Nucl. Med. **47**, 639–647 (2006).
[16]C. Catana, Y. Wu, M. S. Judenhofer, J. Qi, B. J. Pichler, and S. R. Cherry, "Simultaneous acquisition of multislice PET and MR images: Initial results with a MR-compatible PET scanner," J. Nucl. Med. **47**, 1968–1976 (2006).
[17]S. J. Hong, I. C. Song, M. Ito, S. I. Kwon, G. S. Lee, K.-S. Sim, J. T. Rhee, and J. S. Lee, "An investigation into the use of Geiger-mode solid-state photomultipliers for simultaneous PET and MRI acquisition," IEEE Trans. Nucl. Sci. **55**, 882–888 (2008).
[18]H.-P. W. Schlemmer, B. J. Pichler, M. Schmand, Z. Burbar, C. Michel, R. Ladebeck, K. Jattke, D. Townsend, C. Nahmias, P. K. Jacob, W.-D. Heiss, and C. D. Claussen, "Simultaneous MR/PET imaging of the human brain: Feasibility study," Radiology **248**, 1028–1035 (2008).
[19]H. S. Yoon, G. B. Ko, S. I. Kwon, C. M. Lee, M. Ito, I. C. Song, D. S. Lee, S. J. Hong, and J. S. Lee, "Initial results of simultaneous PET/MRI experiments with an MRI-compatible silicon photomultiplier PET scanner," J. Nucl. Med. **53**, 608–614 (2012).
[20]S. Yamamoto, T. Watabe, H. Watabe, M. Aoki, E. Sugiyama, M. Imaizumi, Y. Kanai, E. Shimosegawa, and J. Hatazawa, "Simultaneous imaging using Si-PM-based PET and MRI for development of an integrated PET/MRI system," Phys. Med. Biol. **57**, N1–N13 (2012).

[21]M. S. Judenhofer, H. F. Wehrl, D. F. Newport, C. Catana, S. B. Siegel, M. Becker, A. Thielscher, M. Kneilling, M. P. Lichy, M. Eichner, K. Klingel, G. Reischl, S. Widmaier, M. Rocken, R. E. Nutt, H. J. Machulla, K. Uludag, S. R. Cherry, C. D. Claussen, and B. J. Pichler, "Simultaneous PET-MRI: A new approach for functional and morphological imaging," Nat. Med. **14**, 459–465 (2008).
[22]S. H. Maramraju, S. D. Smith, S. S. Junnarkar, D. Schulz, S. Stoll, B. Ravindranath, M. L. Purschke, S. Rescia, S. Southekal, J.-F. Pratte, P. Vaska, C. L. Woody, and D. J. Schlyer, "Small animal simultaneous PET/MRI: Initial experiences in a 9.4 T microMRI," Phys. Med. Biol. **56**, 2459–2480 (2011).
[23]C. Catana, D. Procissi, Y. Wu, M. S. Judenhofer, J. Qi, B. J. Pichler, R. E. Jacobs, and S. R. Cherry, "Simultaneous *in vivo* positron emission tomography and magnetic resonance imaging," Proc. Natl. Acad. Sci. U. S. A. **105**, 3705–3710 (2008).
[24]S. J. Hong, H. G. Kang, G. B. Ko, I. C. Song, J.-T. Rhee, and J. S. Lee, "SiPM-PET with a short optical fiber bundle for simultaneous PET-MR imaging," Phys. Med. Biol. **57**, 3869–3883 (2012).
[25]C. Kim, G.-C. Wang, and S. Dolinsky, "Multi-pixel photon counters for TOF PET detector and its challenges," IEEE Trans. Nucl. Sci. **56**, 2580–2585 (2009).
[26]S. Seifert, H. T. van Dam, J. Huizenga, R. Vinke, P. Dendooven, H. Löhner, and D. R. Schaart, "Monolithic $LaBr_3$:Ce crystals on silicon photomultiplier arrays for time-of-flight positron emission tomography," Phys. Med. Biol. **57**, 2219–2233 (2012).
[27]J. Y. Yeom, R. Vinke, and C. S. Levin, "Optimizing timing performance of silicon photomultiplier-based scintillation detectors," Phys. Med. Biol. **58**, 1207–1220 (2013).
[28]S. I. Kwon and J. S. Lee, "Signal encoding method for a time-of-flight PET detector using a silicon photomultiplier array," Nucl. Instrum. Methods Phys. Res., Sect. A **761**, 39–45 (2014).
[29]M. S. Judenhofer and S. R. Cherry, "Applications for preclinical PET/MRI," Semin. Nucl. Med. **43**, 19–29 (2013).
[30]G. B. Ko, H. S. Yoon, S. I. Kwon, I. C. Song, D. S. Lee, and J. S. Lee, "New high performance SiPM PET insert to 9.4-T MR scanner for simultaneous PET/MRI studies," J. Nucl. Med. **54**(Suppl. 2), 46 (2013).
[31]G. B. Ko, D. Kim, H. S. Yoon, M. S. Lee, K. Y. Kim, I. C. Song, D. S. Lee, and J. S. Lee, "Evaluation of mutual interference in SiPM based simultaneous PET/MRI operating at animal 7-T MR scanner," J. Nucl. Med. **55**(Suppl. 1), 2140 (2014).
[32]R. Raylman, A. Stolin, B. Hou, and P. Ledden, "Evaluation of an SiPM-based PET/MRI insert," J. Nucl. Med. **56**(Suppl. 3), 314 (2015).
[33]B. Weissler, P. Gebhardt, P. M. Duppenbecker, J. Wehner, D. Schug, C. W. Lerche, B. Goldschmidt, A. Salomon, I. Verel, E. Heijman, M. Perkuhn, D. Heberling, R. M. Botnar, F. Kiessling, and V. Schulz, "A digital preclinical PET/MRI insert and initial results," IEEE Trans. Med. Imaging **34**(11), 2258–2270 (2015).
[34]National Electrical Manufacturers Association, "Performance measurements of small animal positron emission tomographs," NEMA Standards Publication No. NU 4-2008, National Electrical Manufacturers Association, Rosslyn, VA, 2008.
[35]G. B. Ko, H. S. Yoon, S. I. Kwon, C. M. Lee, M. Ito, S. J. Hong, D. S. Lee, and J. S. Lee, "Development of a front-end analog circuit for multi-channel SiPM readout and performance verification for various PET detector designs," Nucl. Instrum. Methods Phys. Res., Sect. A **703**, 38–44 (2013).
[36]S. Yamamoto, J. Satomi, T. Watabe, H. Watabe, Y. Kanai, M. Imaizumi, E. Shimosegawa, and J. Hatazawa, "A temperature-dependent gain control system for improving the stability of Si-PM-based PET systems," Phys. Med. Biol. **56**, 2873–2882 (2011).
[37]G. B. Ko and J. S. Lee, "Performance characterization of high quantum efficiency metal package photomultiplier tubes for time-of-flight and high-resolution PET applications," Med. Phys. **42**, 510–520 (2015).
[38]H. S. Yoon and J. S. Lee, "Bipolar analog signal multiplexing for position-sensitive PET block detectors," Phys. Med. Biol. **59**, 7835–7846 (2014).
[39]M. Ito, J. P. Lee, and J. S. Lee, "Timing performance study of new fast PMTs with LYSO for time-of-flight PET," IEEE Trans. Nucl. Sci. **60**, 30–37 (2013).
[40]H.-J. Im, D. W. Hwang, H. K. Lee, J. Jang, S. Lee, H. Youn, Y. Jin, S. U. Kim, E. E. Kim, Y. S. Kim, and D. S. Lee, "*In vivo* visualization and monitoring of viable neural stem cells using noninvasive bioluminescence imaging in the 6-hydroxydopamine-induced mouse model of Parkinson disease," Mol. Imaging **12**, 224–234 (2013), see http://mi.deckerpublishing.com/index.php/article/in-vivo-visualization-and-monitoring-of-viable-neural-stem-cells-using-noninvasive-bioluminescence-imaging-in-the-6-hydroxydopamine-induced-mouse-model-of-parkinson-disease.
[41]J. S. Lee, K. S. Park, D. S. Lee, C. W. Lee, J.-K. Chung, and M. C. Lee, "Development and applications of a software for functional image registration (FIRE)," Comput. Methods Prog. Biomed. **78**, 157–164 (2005).
[42]A. L. Goertzen, Q. Bao, M. Bergeron, E. Blankemeyer, S. Blinder, M. Cañadas, A. F. Chatziioannou, K. Dinelle, E. Elhami, H.-S. Jans, E. Lage, R. Lecomte, V. Sossi, S. Surti, Y.-C. Tai, J. J. Vaquero, E. Vicente, D. A. Williams, and R. Laforest, "NEMA NU 4-2008 comparison of preclinical PET imaging systems," J. Nucl. Med. **53**, 1300–1309 (2012).
[43]C. C. Constantinescu1 and J. Mukherjee, "Performance evaluation of an Inveon PET preclinical scanner," Phys. Med. Biol. **54**, 2885–2899 (2009).
[44]K. Nagy, M. Tóth, P. Major, G. Patay, G. Egri, J. Häggkvist, A. Varrone, L. Farde, C. Halldin, and B. Gulyás, "Performance evaluation of the small-animal nanoScan PET/MRI system," J. Nucl. Med. **54**, 1825–1832 (2013).